JACS
JOURNAL OF THE AMERICAN CHEMICAL SOCIETY

Article

Biodegradation-Mediated Enzymatic Activity-Tunable Molybdenum Oxide Nanourchins for Tumor-Specific Cascade Catalytic Therapy

Xi Hu, Fangyuan Li, Fan Xia, Xia Guo, Nan Wang, Lili Liang, Bo Yang, Kelong Fan, Xiyun Yan, and Daishun Ling

J. Am. Chem. Soc., **Just Accepted Manuscript** • DOI: 10.1021/jacs.9b13586 • Publication Date (Web): 27 Dec 2019

Just Accepted

is published by the American Chemical Society. 1155 Sixteenth Street N.W., Washington, DC 20036

Biodegradation-Mediated Enzymatic Activity-Tunable Molybdenum Oxide Nanourchins for Tumor-Specific Cascade Catalytic Therapy

Xi Hu,[†,‡,§,o,#,⊥] Fangyuan Li,[†,‡,§,⊥] Fan Xia,[†,‡,⊥] Xia Guo,[†,‡] Nan Wang,[†] Lili Liang,[†] Bo Yang,[‡] Kelong Fan,[Δ,∇] Xiyun Yan,[Δ,∇] Daishun Ling*[,†,‡,§,o]

[†] Institute of Pharmaceutics, College of Pharmaceutical Sciences, Zhejiang University, Hangzhou 310058, China

[‡] Zhejiang Province Key Laboratory of Anti-Cancer Drug Research, College of Pharmaceutical Sciences, Zhejiang University, Hangzhou 310058, China

[§] Hangzhou Institute of Innovative Medicine, College of Pharmaceutical Sciences, Zhejiang University, Hangzhou 310058, China

[o] Key Laboratory of Biomedical Engineering of the Ministry of Education, College of Biomedical Engineering & Instrument Science, Zhejiang University, Hangzhou 310058, China

[#] The First Affiliated Hospital, College of Medicine, Zhejiang University, Hangzhou 310003, China

[Δ] CAS Engineering Laboratory for Nanozyme, Key Laboratory of Protein and Peptide Pharmaceutical, Institute of Biophysics, Chinese Academy of Sciences, 15 Datun Road, Beijing 100101, China

[∇] Academy of Medical Sciences, Zhengzhou University, 40 N Daxue Road, Zhengzhou 450052, China

ABSTRACT: Recent advances in nanomedicine have facilitated the development of potent nanomaterials with intrinsic enzyme-like activities (nanozymes) for cancer therapy. However, it remains great challenges to fabricate smart nanozymes that precisely perform enzymatic activity in tumor microenvironment without inducing off-target toxicity to surrounding normal tissues. Herein, we report on designed fabrication of biodegradation-medicated enzymatic activity-tunable molybdenum oxide nanourchins (MoO_{3-x} NUs), which selectively perform therapeutic activity in tumor microenvironment via cascade catalytic reactions, while keep normal tissues unharmed due to their responsive biodegradation in physiological environment. Specifically, the MoO_{3-x} NUs first induce catalase (CAT)-like reactivity to decompose hydrogen peroxide (H_2O_2) in tumor microenvironment, producing a considerable amount of O_2 for subsequent oxidase (OXD)-like reactivity of MoO_{3-x} NUs; a substantial cytotoxic superoxide radical ($^{\cdot}O_2^-$) is thus generated for tumor cell apoptosis. Interestingly, once exposed upon neutral blood or normal tissues, MoO_{3-x} NUs rapidly lose the enzymatic activity via pH-responsive biodegradation and are excreted in urine, thus ultimately ensuring safety. The current study demonstrates a proof of concept of biodegradation-medicated in vivo catalytic activity tunable nanozymes for tumor specific cascade catalytic therapy with minimal off-target toxicity.

INTRODUCTION

Chemically-engineered functional nanomaterials with intrinsic biological activities, exerting potent anti-cancer therapeutic effects via, e.g., generation of reactive oxygen species (ROS),[1-6] selective ion leaching,[7,8] or radiosensitizing effects,[9] represent a new era of cancer nanomedicines. In particular, nanomaterials mimicking oxidoreductase including peroxidase (POD), oxidase (OXD), and catalase (CAT), so called "Nanozyme", have sparked an increasing interest because they can fine-tune the intracellular biochemical reactions for satisfactory tumor diagnostic and/or therapeutic outcomes.[1,10-18] However, for in vivo applications, the undesired off-target activity of nanozyme can lead to unpredictable toxicity.[1,19,20] Hence, it is highly desirable to confine the catalytic reaction-based therapeutic effects of nanozymes exclusively in tumors, while being inert to normal tissues, which is extremely valuable but yet remains a significant challenge.

In nature, the activities of biological enzymes are correlated with their defined structures.[21,22] For instance, the enzymatic effect of the antiretroviral enzyme APOBEC3G for viral cDNA replication can be suppressed once they are degraded by the proteasome.[23] We are, therefore, inspired to explore the on/off-switchable activity of nanozymes via the biodegradation-mediated regulation of their nanostructures. It is reported that the branched nanomaterials own large population of atoms at their corners and edges, thus gaining large active surface area with high reactivity.[24-26] For example, Mn_3O_4 nanoflowers exhibit much higher CAT-, glutathione

Scheme 1. Schematic illustration of biodegradation-medicated enzymatic activity-tunable molybdenum oxide nanourchins (MoO_{3-x} NUs) with the highly specific toxicity to tumor tissues via a multi-enzyme stepwise cascade catalysis in acidic tumor microenvironment, while leaving normal tissues unharmed due to their pH-responsive biodegradation and subsequent renal excretion in physiological environment.

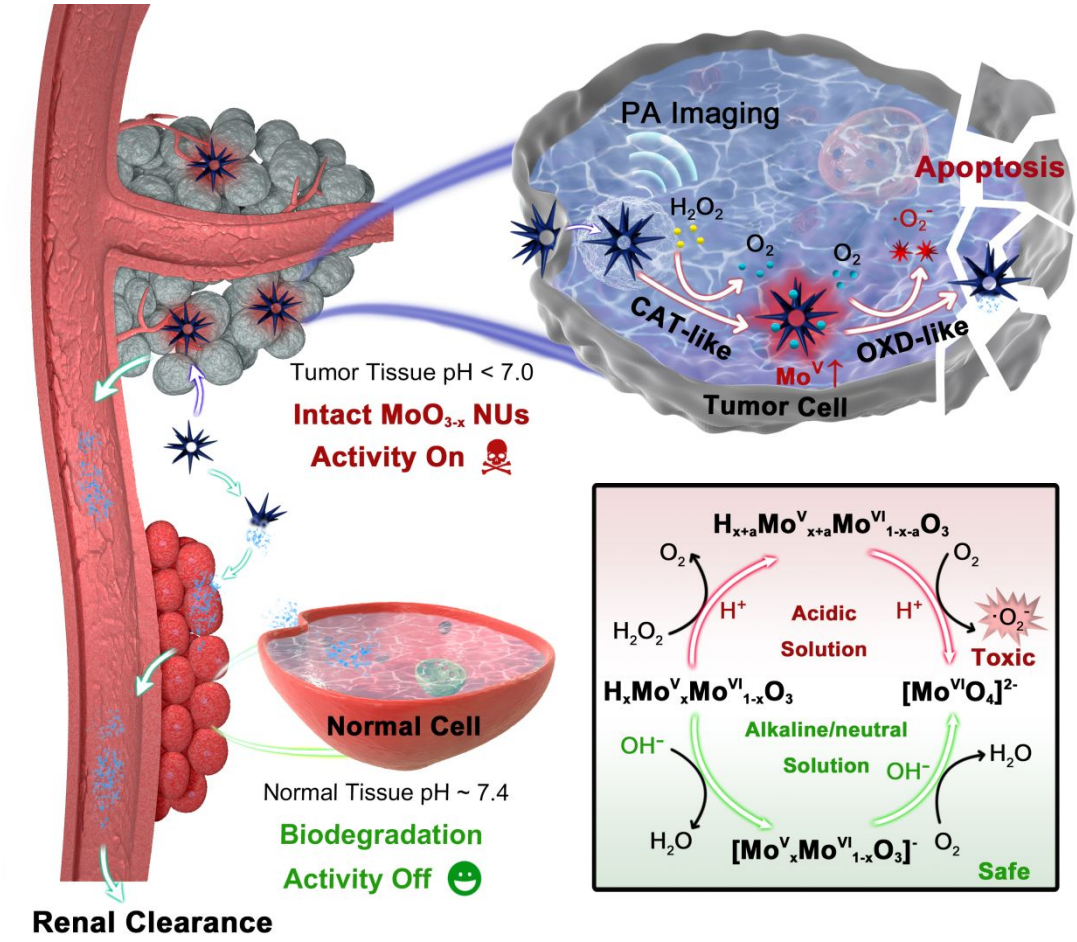

peroxidase (GPx)-, and superoxide dismutase (SOD)-like catalytic activities than other shaped Mn_3O_4 nanomaterials (e.g., flakes, cubes, polyhedra, and hexagonal plates).[27] In this consideration, we envision that the dynamic biodegradation-mediated structural regulation of nanozymes between pathological and physiological conditions can hopefully achieve the concurrent tumor selective catalytic therapy and great biocompatibility with surrounding normal tissues.

Herein, we report for the first time that MoO_{3-x} nanourchins (NUs) with a structure-dependent enzymatic activity can perform highly specific cascade catalytic activity exclusively against tumor, while leaving normal tissues unharmed due to their rapid biodegradation in physiological environment. In our design, benefiting from the large active surface area and high proportion of active Mo^V atoms, MoO_{3-x} NUs reveal the excellent CAT-like activity in acidic tumor microenvironment, generating abundant O_2 via decomposing H_2O_2; and subsequently, the OXD-like activity of MoO_{3-x} NUs is activated to transfer electrons to O_2 and form cytotoxic superoxide radicals ($^{\bullet}O_2^-$) (Scheme 1). However, on exposure to a physiological environment (pH~7.4), MoO_{3-x} NUs would rapidly lose the enzymatic activity via the pH-responsive biodegradation, whose products are proved to be renal clearable and biocompatible molybdate ions.

RESULTS AND DISCUSSION

Synthesis and Characterization of MoO_{3-x} NUs. Initially, spherical MoO_{3-x} nanoparticles were synthesized via uniformly heating of the reactants at 100 ˚C (Figure S1). Then, the MoO_{3-x} NUs were obtained after a solvothermal reaction at 160 ˚C (Figure 1a). As revealed by transmission microscopy (TEM), the NUs are hollow and covered with spikes (Figures 1b and S2). The average core size of the NUs is 142.8±13.3 nm, and the surface spikes are 15.4±3.3 nm in cross-sectional diameter and 116.7±24.6 nm in length (Nano Measure Software). As identified by X-ray diffraction (XRD) analysis, the MoO_{3-x} NUs are primarily composed of hexagonal MoO_{3-x} (PDF no. 21-0569; Figure S3). Besides, Mo 3d X-ray photoelectron spectroscopy (XPS) spectrum reveals the presence of Mo^{VI} species (BE at 235.8 eV and 232.6 eV) and Mo^V (BE at 234.3 eV and 231.5 eV),[28-30] and the proportion of Mo^V species in MoO_{3-x} NUs is calculated to be ~47.0% (Figure 1c). Furthermore, the Raman spectrum demonstrates the existence of H^+ in MoO_{3-x} NUs (Figure S4), indicating that the composition is $H_x(Mo^V_x)(Mo^{VI}_{1-x})O_3$ (x=0.47, abbreviated as MoO_{3-x}).[31-33] It

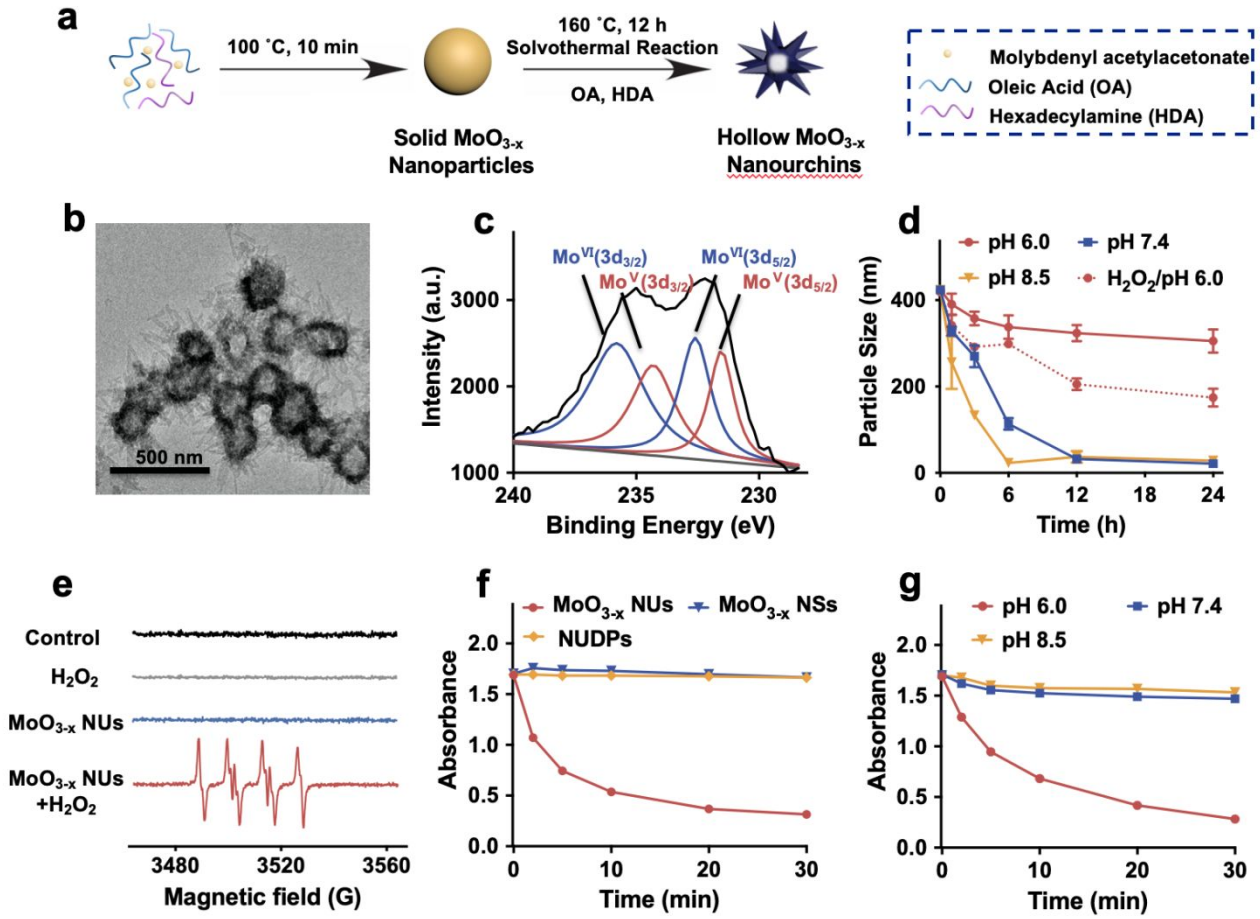

Figure 1. Synthesis and characterization of MoO_{3-x} NUs. (a) Schematic illustration of the synthesis process of MoO_{3-x} NUs. (b) The TEM image of MoO_{3-x} NUs. (c) The Mo XPS spectrum of MoO_{3-x} NUs. (d) Particle sizes of MoO_{3-x} NUs at various time points after incubation in PBS (pH 6.0, pH 7.4, and pH 8.5), 1 mM H_2O_2/PBS (pH 6.0), and distilled water. (e) Electron spin resonance (ESR) spectra of MoO_{3-x} NUs in the presence of BMPO and H_2O_2 (1 mM). (f) UV-Vis absorbance of 1,3-diphenylisobenzofuran (DPBF) in distilled water/ethanol solutions with MoO_{3-x} NUs, MoO_{3-x} nanosheets (NSs), or NUDPs (Mo, 20 μg; λ=410 nm). (g) UV-Vis absorbance of DPBF in PBS (pH 6.0, pH 7.4, and pH 8.5)/ethanol solutions with MoO_{3-x} NUs (Mo, 20 μg; λ=410 nm).

is speculated that the etching process is originated from the central part with the assistant of oleic acid (OA) and hexadecylamine (HDA) as etching agents, accompanied by a reduction in the Mo species.[34,35]

pH-Responsive Biodegradation of MoO_{3-x} NUs. 1,2-distearoyl-sn-glycero-3-phosphoethanolamine-N-[methoxy (polyethylene glycol)-2000] ($DSPE\text{-}PEG_{2000}$) was employed for surface modification, as confirmed by thermogravimetric analysis (TGA) and Fourier transform infrared (FT-IR) spectra analysis (Figure S5). Moreover, MoO_{3-x} NUs could be easily degraded in aqueous solution containing H_2O_2 or OH^-, accompanied by color fading (Figure S6). As shown in Figure 1d, the particle size of MoO_{3-x} NUs decreases rapidly in both neutral and alkaline phosphate buffer saline (PBS). Interestingly, the size decrease is very slow under acidic conditions but can be accelerated with the added H_2O_2. Moreover, the Mo XPS spectrum of MoO_{3-x} NUs degradation products (NUDPs) confirms the oxidation of Mo^V species into Mo^{VI} species (Figure S7).[36-38] Furthermore, the pH dependent Mo ion release profiles as measured by an inductively coupled plasma mass spectrometer (ICP-MS) are consistent with the trends of particle size changes as shown in Figure 1d, implying that the NUDPs should be molybdate ions (Figure S8). From the UV-Vis-NIR spectrum, MoO_{3-x} NUs show a broad absorption band in the NIR region, which dramatically vanishes under the neutral, alkaline, and H_2O_2 conditions (Figure S9). According to the pH-responsive biodegradation, it is speculated that small ions such as H^+ are implanted into the urchin-like nanostructure, accompanied by the partial reduction of Mo species with the assistant of OA and HDA as etching agents.[31]

Biodegradation Regulated Enzymatic Activity and Catalytic Mechanism of MoO_{3-x} NUs. We further investigated the enzyme-like activity of MoO_{3-x} NUs. The gas bubbles and O_2 concentration profiles indicate that the O_2 production capability of MoO_{3-x} NUs in acidic PBS is much stronger than that in neutral or alkaline PBS, demonstrating the decreased CAT-like activity of MoO_{3-x} NUs induced by the pH-responsive biodegradation in neural and alkaline environments (Figure S10). Also, we found that o-phenylenediamine (OPD) and 3,3',5,5'-

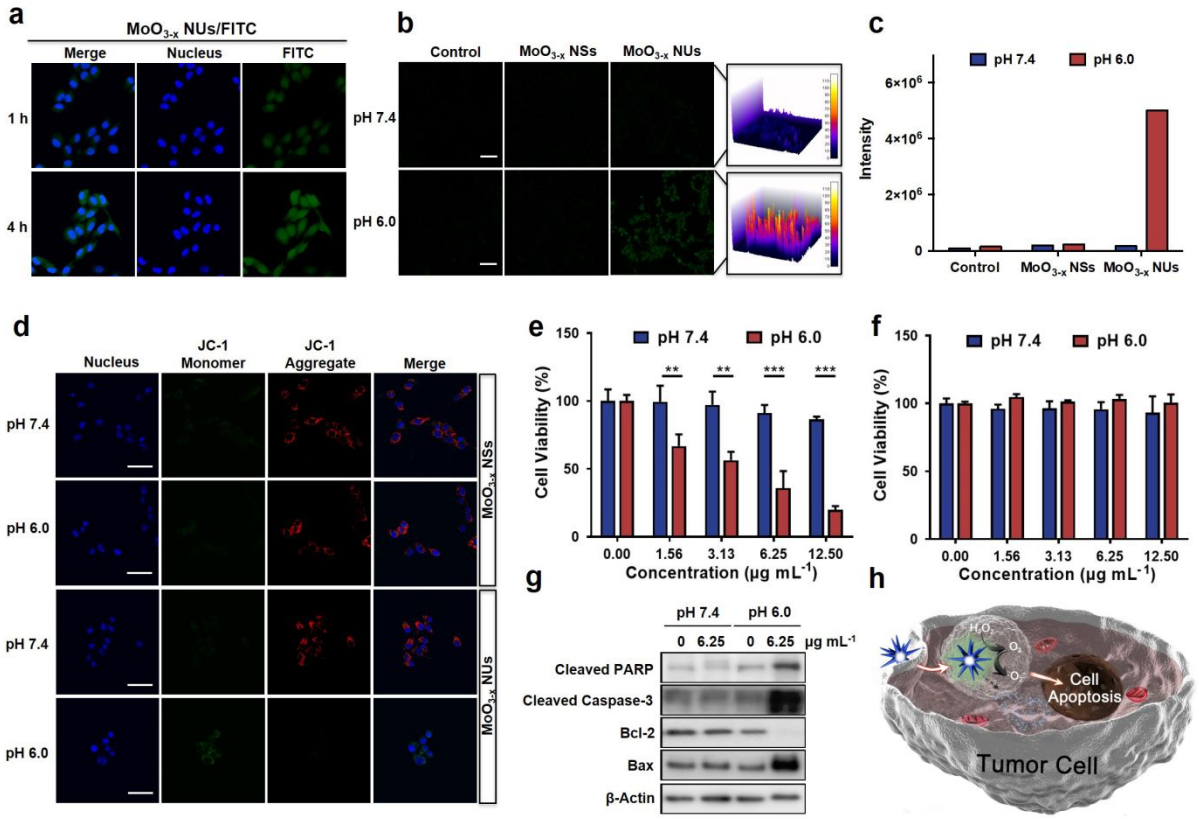

Figure 2. pH-Dependent cell death caused by MoO_{3-x} NUs with biodegradation-regulated catalytic activity. (a) Representative confocal laser scanning microscopic (CLSM) images of B16 tumor cells after incubation with DMEM (pH 6.0) containing MoO_{3-x} NUs/FITC for 1 h and 4 h. (b) Representative CLSM images of the degree of intracellular oxidative stress via DCFH-DA staining. Right panel, 3D mapping of intracellular fluorescence. Cells were treated with DMEM containing MoO_{3-x} NUs or MoO_{3-x} NSs (Mo, 6.25 μg mL^{-1}) at pH 7.4 and pH 6.0, respectively. Scale bar=100 μm. (c) Quantitative analysis of intracellular ROS fluorescence intensity. (d) Effect of MoO_{3-x} NUs or MoO_{3-x} NSs (Mo, 6.25 μg mL^{-1}) on mitochondrial membrane potential ($\Delta\psi_m$) in B16 cells. Red JC-1 aggregate indicates mitochondria with a normal membrane potential, and the green JC-1 monomer means the mitochondria with a depolarized membrane (impaired mitochondria). Scale bar=50 μm. (g) Effects of MoO_{3-x} NUs on the expression of cleaved PARP, cleaved caspase-3, Bax, and Bcl-2. Cytotoxicity of MoO_{3-x} NUs (e) or MoO_{3-x} NSs (f) to B16 tumor cells after incubation in DMEM at pH 7.4 and pH 6.0. (h) Schematic illustration of MoO_{3-x} NUs-induced anti-tumor mechanism. *P<0.05, **P<0.01, ***P<0.001.

tetramethylbenzidine (TMB) could be oxidized by MoO_{3-x} NUs in the presence of H_2O_2 (Figure S11). To elucidate the catalytic mechanism of MoO_{3-x} NUs, the type of free radical products was determined via electron spin resonance (ESR) with 5-tertbutoxycarbonyl-5methyl-1-pyrroline N-oxide (BMPO) as the specific spin trap reagent (Figure 1e), which shows that $^{\cdot}O_2^-$ is the unique product in the MoO_{3-x} NUs-catalyzed reaction. These results indicate that MoO_{3-x} NUs can efficiently yield $^{\cdot}O_2^-$, in sharp contrast to either NUDPs or MoO_{3-x} nanosheets (NSs; Figure S12).[31] Moreover, 1,3-diphenylisobenzofuran (DPBF) and methylene blue (MB) were applied to further verify the ROS products of the reaction, and the ROS produced by MoO_{3-x} NUs is verified to be $^{\cdot}O_2^-$ rather than $^1O_2$[39] or ·OH (Figures 1f, S13 and S14), indicating the OXD-like activity of MoO_{3-x} NUs.[10,11] Moreover, it is noteworthy that the proper amount of H_2O_2 can increase the proportion of Mo^V species on the surface of MoO_{3-x} NUs (from 47.0% to 53.3%; Figures 1c and S15), enhancing the OXD-like activity of MoO_{3-x} NUs (Scheme 1); while the over excess amount of H_2O_2 or long incubation time leads to the oxidization of Mo^V species and consequently decrease the OXD-like activity of MoO_{3-x} NUs (Figure S16). These results suggest that, MoO_{3-x} NUs decompose the H_2O_2 into O_2 with the increasing of the proportion of Mo^V species. Subsequently, the generated O_2 is easily adsorbed on the large active surface of MoO_{3-x} NUs and being transformed into $^{\cdot}O_2^-$ by Mo^V via the cascade reactions, revealing the activated OXD-like activity. The active electron for the "O_2–$^{\cdot}O_2^-$" reaction is probably derived from the intervalence charge-transfer transition between Mo^V to Mo^{VI} on the surface of MoO_{3-x} NUs.[40-43] In contrast, no ROS product of MoO_{3-x} NSs (containing 37% Mo^V species)[31] was detected in the same procedure (Figures 1f, S12, S14 and S17). The high ROS production efficiency of MoO_{3-x} NUs is likely attributed to their large active surface area and the high proportion of Mo^V atoms exposed at the sites of surface defects.[26,44,45]

During the pH-responsive biodegradation process in neutral and alkaline environments, Mo^V species of MoO_{3-x} NUs are oxidized and depleted, resulting in the vanishment of the CAT-like and OXD-like activities (Figures 1f,g and S10, S18). Nevertheless, MoO_{3-x} NUs maintain great enzymatic activity after storage in distilled water for 7 d

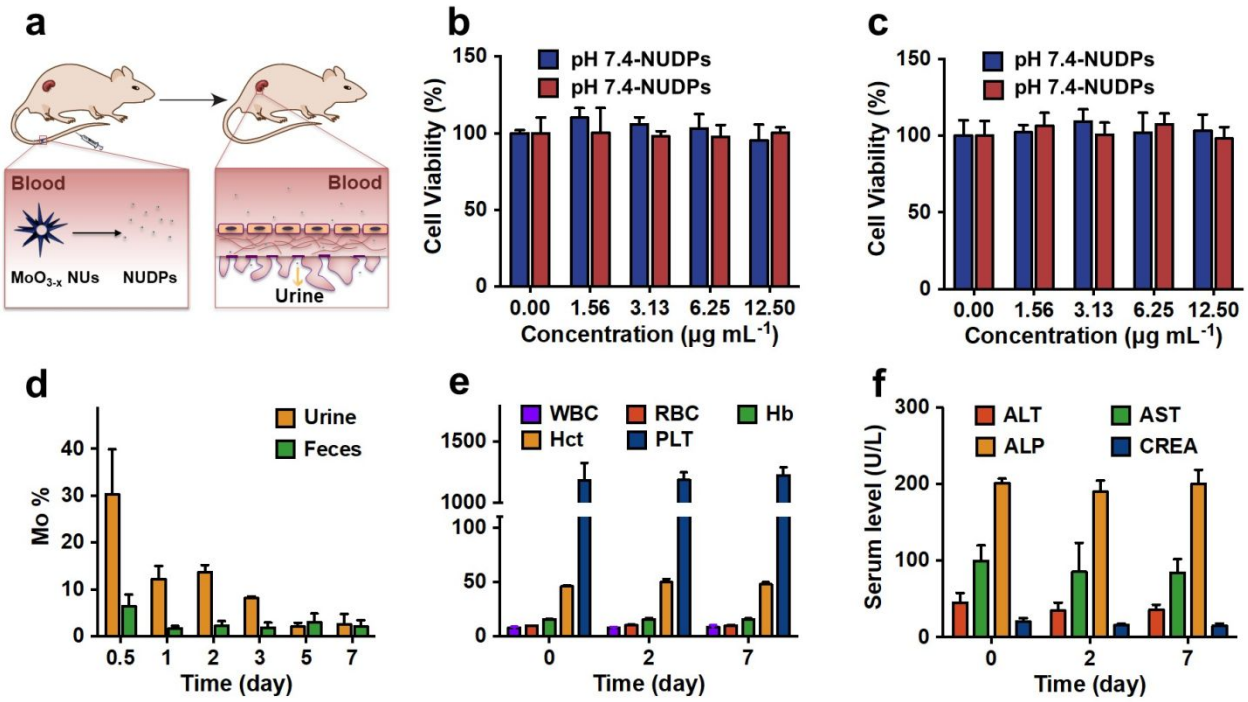

Figure 3. The safety evaluation of MoO_{3-x} NUs after biodegradation once entering circulation system. (a) Illustration of the in vivo fate of MoO_{3-x} NUs after intravenous administration. On exposure to neutral blood or normal tissues, MoO_{3-x} NUs biodegrade into safe ions, which then are excreted via kidney, thus ensuring great biocompatibility. (b,c) Cytotoxicity of NUDPs to B16 tumor cells (b) and L02 normal cells (c) at pH 7.4 and pH 6.0. (d) Mo in urine and feces of mice at indicated time points after intravenous injection of MoO_{3-x} NUs (n=6). (e) Hematology data, including white blood cells (10^9 L^{-1}, WBC), red blood cells (10^{12} L^{-1}, RBC), hemoglobin (g L^{-1}, Hb), hematocrit (%, Hct), platelets (10^9 L^{-1}, PLT) of mice at 0 d, 2 d, and 7 d post intravenous injection with MoO_{3-x} NUs (n=6). (f) Blood biochemical tests, including alanine aminotransferase (ALT), aspartate aminotransferase (AST), alkaline phosphatase (ALP), and creatinine (CREA) on mice at 0 d, 2 d, and 7 d post intravenous injection with MoO_{3-x} NUs (n=6).

(Figure S19), and could be used for at least three cycles (Figure S20), indicating the stability and reusability of MoO_{3-x} NUs.

Biodegradation Regulated in Vitro Cytotoxicity and Cell Death Mechanism. Firstly, the cellular uptake of both MoO_{3-x} NUs and MoO_{3-x} NSs was confirmed by confocal laser scanning microscopy (CLSM; Figures 2a and S21). As to enzyme-like MoO_{3-x} NUs, they could effectively consume tumor intracellular high levels of H_2O_2[46] and yield excessive amounts of $^{\cdot}O_2^-$ to elicit irreversible biomolecules and membrane damage.[47-49] To further investigate the biodegradation regulated catalytic activity at the cellular levels, following cellular studies including ROS levels, mitochondrial membrane potential, cytotoxicity, and apoptosis, were conducted at both acidic condition (pH 6.0) and neutral condition (pH 7.4). The tumor cells incubated with MoO_{3-x} NUs or MoO_{3-x} NSs were stained with 2,7-dichlorofluorescin diacetate (DCFH-DA) to visualize the intracellular ROS levels (Figure 2b,c). Interestingly, the fluorescence intensity of MoO_{3-x} NUs-treated cells increases sharply with a reduction in pH because the $^{\cdot}O_2^-$ is the primary product at acidic pH; while the $^{\cdot}O_2^-$ generation pathway is blocked at a neutral pH owing to the rapid oxidative biodegradation of MoO_{3-x} NUs (Scheme 1). Also, cells treated with MoO_{3-x} NUs at pH 6.0 reveal markedly higher intracellular ROS levels than those treated with MoO_{3-x} NSs. Moreover, JC-1 staining analysis shows that the excess generation of $^{\cdot}O_2^-$ by MoO_{3-x} NUs in an acidic environment impacts the mitochondrial membrane potential ($\Delta\psi_m$) and leads to mitochondrial membrane disruption (Figure 2d). Consequently, the MoO_{3-x} NUs exhibit significant cytotoxicity in acidic media, while no obvious cell death is observed in neutral media (Figure 2e). In contrast, there is negligible cytotoxicity of MoO_{3-x} NSs to tumor cells (Figure 2f), indicating the superior cytotoxicity of MoO_{3-x} NUs is based on their unique morphology as well as abundant Mo^V species. Furthermore, western blot analysis was performed to verify the expression of anti-apoptotic and apoptotic proteins in tumor cells upon exposure to MoO_{3-x} NUs (Figure 2g) or MoO_{3-x} NSs (Figure S22). The expression levels of cleaved PARP, cleaved caspase-3 as well as the Bax/Bcl-2 ratio significantly increase in B16 tumor cells incubated in DMEM at pH 6.0. Taken together, we can conclude that once internalized in acidic lysosomes of tumor cells, the MoO_{3-x} NUs induce mitochondrial dysfunction, the caspase-3/PARP pathway activation, and cell damage through catalyzing a "$H_2O_2 \rightarrow O_2 \rightarrow {}^{\cdot}O_2^-$" successive reaction (Figure 2h).

Biodegradation Ensured Safety Profiles of MoO_{3-x} NUs. Since the toxic $^{\cdot}O_2^-$ generation of MoO_{3-x} NUs can be significantly inhibited in neutral solutions due to rapid biodegradation (Figures 1g and 2), the NUDPs are expected to be biocompatible and renal clearable (Figure

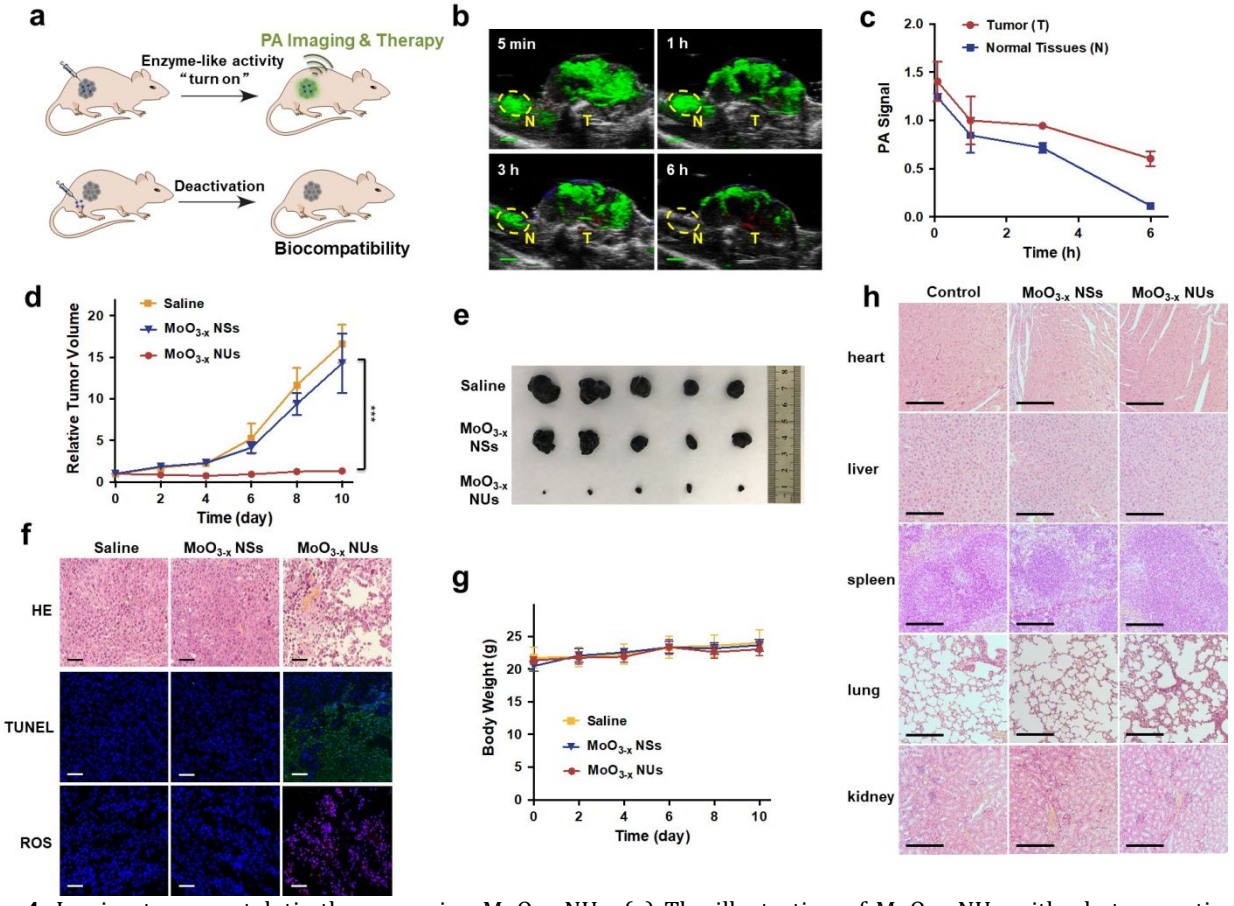

Figure 4. In vivo tumor catalytic therapy using MoO_{3-x} NUs. (a) The illustration of MoO_{3-x} NUs with photoacoustic (PA) signals and therapeutic activity in tumor regions, and their silencing in marginal normal tissues. (b) Merged ultrasound (US) and PA imaging of a BALB/c nude mouse harboring the B16 tumor xenograft at 5 min, 1 h, 3 h, and 6 h post in situ injection of MoO_{3-x} NUs. T, tumor; N, normal tissue. Scale bar=2 mm. (c) The mean of highest PA signal values at various time points of corresponding PA imaging (b; λ=910 nm). (d,e) Tumor growth curves (d) and image of tumors (e) of BALB/c nude mice harboring the B16 tumor xenograft after different treatments (n=5). (f) Hematoxylin and eosin (HE) staining, terminal deoxynucleotidyl transferase dUTP nick end labeling (TUNEL) staining, and ROS staining of tumors after different treatments. Scale bar=50 μm. (g) Body weights of BALB/c nude mice harboring the B16 tumor xenograft during different treatments. (h) HE staining of various organs in BALB/c nude mice harboring the B16 tumor xenograft after different treatments. Scale bar=200 μm. *P<0.05, **P<0.01, ***P<0.001.

3a). The safety of MoO_{3-x} NUs was investigated both in vitro and in vivo. We find that the NUDPs show negligible cytotoxicity to both tumor cells (Figure 3b) and normal cells (Figure 3c). Also, after intravenous injection, the majority of MoO_{3-x} NUs are rapidly biodegraded into biocompatible NUDPs and then cleared from blood circulation by urinary excretion (Figure 3d), thus ensuring safety. Consequently, both hematological test results (Figure 3e) and blood biochemical test results (Figure 3f) show no obvious change after the treatment of MoO_{3-x} NUs, indicating the MoO_{3-x} NUs are highly biocompatible in vivo owing to the responsive biodegradation.

In Vivo Tumor Specific Catalytic Activity of MoO_{3-x} NUs. As a localized surface plasmon resonance (LSPR) nanomaterial, MoO_{3-x} NUs exhibit high photoacoustic (PA) signals in the 870-950 nm range,[33,50] which, however, become diminished after biodegradation (Figure S23). Therefore, we performed PA imaging to monitor the in vivo fate of MoO_{3-x} NUs in the tumor and the adjacent normal tissue (Figure 4a). PA imaging was conducted at 5 min, 1 h, 3 h, and 6 h after in situ injection (Figure 4b). Interestingly, the PA signal intensity in the normal tissue displays a sharp time-dependent reduction and almost vanishes at 6 h post-injection. However, the PA signal intensity at the tumor site remains high for more than 6 h (Figure 4c). The slow decrease of PA signal in the tumor tissue is attributed to the consumption of MoO_{3-x} NUs in the "$H_2O_2 \rightarrow O_2 \rightarrow {}^{\cdot}O_2^-$" cascade reaction. Moreover, the Mo levels in both tumor tissues and muscles were quantified by ICP-MS. As shown in Figure S24, the time-dependent decrease of Mo levels is consistent with PA results, owing to the loss of Mo ions following the consumption of MoO_{3-x} NUs.[51] It implies that MoO_{3-x} NUs can achieve long-term tumor retention, facilitating tumor imaging and therapy.

We further assessed the tumor therapeutic effect of MoO_{3-x} NUs in vivo. As shown in Figure 4d,e, the tumor inhibition rate of MoO_{3-x} NUs is as high as 92% after treatment. And it is worth mentioning that the mean relative tumor volume of the MoO_{3-x} NUs-treated mice is 10.8-fold less than that of the MoO_{3-x} NSs-treated mice.

Hematoxylin & eosin (HE) staining and terminal deoxynucleotidyl transferase dUTP nick end label (TUNEL) staining reveal a markedly higher apoptotic rate in the tumor tissue upon MoO_{3-x} NUs treatment (Figure 4f). Furthermore, the ROS level in MoO_{3-x} NUs-treated tumors is significantly higher than that in MoO_{3-x} NSs-treated tumors, deriving from the in vivo $^{\cdot}O_2^-$ overproduction triggered by MoO_{3-x} NUs. Moreover, body weights of mice (Figure 4g) and HE staining of various organs after treatment (Figure 4h), as well as the hematological and blood biochemical tests results after intramuscular injection (Figure S25) reveal no obvious toxicity of biodegradable MoO_{3-x} NUs.

CONCLUSION

In summary, we have developed a biodegradation-medicated in vivo catalytic activity tunable nanozyme, MoO_{3-x} NUs, which not only precisely perform highly tumor-specific cascade catalytic therapy, but also leave normal tissues unharmed due to their rapid and responsive biodegradation under normal physiological conditions. In the acidic tumor microenvironment, MoO_{3-x} NUs with the CAT-like activity and OXD-like activity mediate a "$H_2O_2 \rightarrow O_2 \rightarrow {}^{\cdot}O_2^-$" cascade reaction to cause tumor cells apoptosis and significantly inhibit the tumor growth. However, on exposure to the physiological environment (pH~7.4), MoO_{3-x} NUs are easily oxidized and biodegraded into renal clearable ion species with the vanishment of enzymatic activity. We explored pH-responsive biodegradation-mediated structural regulation to fine-tune the enzymatic activity of MoO_{3-x} NUs for tumor specific cascade catalytic therapy with minimal off-target toxicity. Therefore, harnessing the unique features and regulating the catalytic reactivities of engineered nanomaterials would facilitate the rational design of smart nanozymes to regulate their in vivo performances.

EXPERIMENTAL SECTION

Materials. Molybdenyl acetylacetonate, hexadecylamine, 1-octadecene, 1,3-diphenylisobenzofuran (DPBF), 3,3',5,5'-tetramethylbenzidine (TMB) and methylene blue (MB) were purchased from Aladdin Industrial Inc. (Shanghai, China). 5-tertbutoxycarbonyl-5methyl-1-pyrroline N-oxide (BMPO) was purchased from APExBIO (Houston, USA). Oleic acid (90%) was purchased from Sigma-Aldrich Co. (St. Louis, MO, USA). Chloroform, cyclohexane, ethanol, hydrochloric acid (HCl), sodium hydroxide (NaOH), and hydrogen peroxide (H_2O_2) were purchased from Sinopharm Chemical Reagent Co., Ltd. (Shanghai, China). 1,2-distearoyl-sn-glycero-3-phosphoethanolamine-N-[methoxy (polyethylene glycol)-2000] (DSPE-PEG_{2000}) was obtained from Shanghai Advanced Vehicle Technology Pharmaceutical Co., Ltd. (Shanghai, China). Fetal bovine serum was obtained from Sijiqing Biologic Co., Ltd. (Hangzhou, China). Dulbecco's modified Eagle medium (DMEM) was obtained from Jinuo Biomedical Technology Co., Ltd. (Hangzhou, China). Cell Counting Kit-8, Reactive Oxygen Species Assay Kit (DCFH-DA), Mitochondrial Membrane Potential Assay Kit (JC-1), and Hoechst 33342 staining solution were purchased from Beyotime Biotechnology. (Shanghai, China).

Synthesis of MoO_{3-x} Nanourchins (NUs). 40 mg of molybdenyl acetylacetonate, 0.20 g of hexadecylamine (HDA), and 2.0 mL of oleic acid (OA) were added to 8 mL of 1-octodecene, which were then uniformly heated at 100 °C for 10 min. The mixture (as a pre-heating product) was transferred into a Teflon-lined autoclave (15 mL), which was then maintained at 160 °C for 12 h. After centrifugation (11000 rpm, 10 min), the precipitate was washed three times with ethanol and finally dispersed in chloroform.

Synthesis of MoO_{3-x} Nanosheets (NSs). In a typical procedure,[31] 0.5 g of ammonium molybdate was dissolved in 26 mL of deionized water and 2.4 mL of HCl (1 M). Then 1.6 g of oleylamine was dissolved in 8 mL of cyclohexane, and added into ammonium molybdate solution. The milky emulsion was then transferred into a Teflon-lined autoclave (50 mL) and maintained at 180 °C for 12 h. The blue MoO_{3-x} NSs were extracted by adding cyclohexane and then precipitated by adding the double volume of ethanol. After centrifugation (11000 rpm, 10 min), the precipitate was washed three times with ethanol and finally dispersed in chloroform.

Surface Modification of MoO_{3-x} NUs and MoO_{3-x} NSs. DSPE-PEG_{2000} was used to transform MoO_{3-x} NUs or MoO_{3-x} NSs into aqueous phase. Briefly, 20 mg of DSPE-PEG_{2000} and 2 mg of MoO_{3-x} NUs or MoO_{3-x} NSs were mixed in chloroform under magnetic stirring. The dispersion was dried by rotary evaporation under vacuum for 1 h before adding distilled water. Excess surfactants were then removed by centrifugation.

Preparation of MoO_{3-x} NUs Degradation Products (NUDPs). Complete degradation would be achieved by dispersing MoO_{3-x} NUs in NaOH solution (1 M) at 60 °C for 24 h (Mo, 1 mg mL^{-1}). The NUDPs were then obtained after lyophilization.

Characterization. Transmission electron micrograph (TEM) images were taken using a HITACHI HT7700 at a voltage of 120 kV. Elemental analysis of MoO_{3-x} NUs was studied using a FEI Tecnai G2 F20 S-TWIN field-emission microscope. The molybdenum element concentration was determined by a PerkinElmer NexION 300XX inductively coupled plasma mass spectrometer (ICP-MS). X-ray powder diffraction (XRD) pattern was collected on a X-pert Powder (PANalytical B.V., Holland). X-ray photoelectron spectroscopy (XPS) analysis was performed on a VG Scientific ESCALAB Mark II spectrometer. Raman spectrum was measured on a LabRAM HR Evolution (HORIBA France SAS, France). Dynamic light scattering (DLS) was conducted on a Zetasizer Nano ZS90 equipment (Malvern instruments, UK).

The pH-Dependent Behavior of MoO_{3-x} NUs. After dispersing the MoO_{3-x} NUs in PBS (pH 6.0, pH 7.4, and pH 8.5; 10 mM) or 1 mM H_2O_2/PBS (pH 6.0, 10 mM), the size, appearance, and UV-Vis-NIR absorption of MoO_{3-x} NUs were studied at various time points. In addition, the Mo ion release was conducted after placing MoO_{3-x} NUs (Mo, 80 μg) in a dialysis tube (MWCO 3500 Da) and dialyzing against 10 mL of PBS (pH 6.0, pH 7.4, and pH 8.5; 10 mM) or 1 mM H_2O_2/PBS (pH 6.0, 10 mM) at 37 °C. The release medium was all taken out and the same volume of fresh medium was added at various time points. The amount of released Mo was directly quantified using the ICP-MS.

Catalase (CAT)-Like Activity. 20 μL of MoO_{3-x} NUs (1 mg mL^{-1}) and 1 μL of H_2O_2 (1 M) were added into 1 mL of PBS (pH 6.0, pH 7.4, and pH 8.5; 10 mM). After incubation at 40 °C, the CAT reactions were recorded by photography.

Measurement of O_2 Production. 240 μL of MoO_{3-x} NUs (1 mg mL^{-1}) and 60 μL of H_2O_2 (1 M) were added into 6 mL of PBS (pH 6.0, pH 7.4, and pH 8.5; 10 mM), the oxygen generation ability was evaluated by an oxygen electrode on Dissolved Oxygen Meter JPB-607 (Shanghai INESA Scientific Instrument, China).

Oxidase (OXD)-Like Activity. 80 μL of MoO_{3-x} NUs (1 mg mL^{-1}) or MoO_{3-x} NSs (1 mg mL^{-1}), and 200 μL of OPD (50 mM) were added into HAc/NaAc buffer solution (pH 4.5, 0.1 M; the total volume of mixture is 2 mL) with or without 4 μL of H_2O_2 (1 M). The reaction was measured at certain time points by a UV-Vis spectroscopy at 450 nm. In addition, TMB (1 mM) was also employed to verify the OXD-like activity of MoO_{3-x} NUs and MoO_{3-x} NSs, and the reaction was measured at certain time points by a UV-Vis spectroscopy at 652 nm. After incubated with H_2O_2 (0.1 mM, 1 mM, and 10 mM) for 1 h or 1 mM H_2O_2 at different times (1 h, 3 h, and 6 h), MoO_{3-x} NUs were collected by centrifugation (11000 rpm, 10 min) and washed by water to remove excess H_2O_2. Moreover, the residual H_2O_2 was measured using UV-Vis spectroscopy based on the starch-iodine complex. Briefly, 0, 0.20, 0.40, 0.60, 0.80 and 1.00 mL of H_2O_2 solution (10 μg mL^{-1}) was diluted to 5 mL using distilled water respectively, and 1.0 mL of HCl (10%), 0.5 mL of sodium chloride solution (200 mg mL^{-1}), 0.3 mL of potassium iodide solution (10 mg mL^{-1}) and 0.2 mL starch solution (10 mg mL^{-1}) were sequentially added. After incubation for 40 min, the absorbance was measured by a UV-Vis spectroscopy at 560 nm, and a standard curve in the range of 0-60 nmol mL^{-1} was plotted with H_2O_2 concentration versus UV absorbance. The amount of residual H_2O_2 in MoO_{3-x} NUs was measured directly using the standard curve. Furthermore, to study the OXD-like activity, 80 μL of MoO_{3-x} NUs (1 mg mL^{-1}) and 200 μL of OPD (50 mM) were added into 2 mL of HAc/NaAc buffer solution (pH 4.5, 0.1 M). The absorbance of the OXD reaction was detected at a certain time by a UV-Vis spectroscopy at 450 nm.

ESR measurements. For $^{\cdot}O_2^-$ detection, the PBS (pH 5.0, 25 mM) containing BMPO (25 mM), H_2O_2 (1 mM), and MoO_{3-x} NUs or MoO_{3-x} NSs (20 μg mL^{-1}) was prepared. ESR spectra were recorded after 3 min incubation.

In Vitro $^{\cdot}O_2^-$ Detection. DPBF was used to detect the in vitro generation of ROS including $^{\cdot}O_2^-$ and $^1O_2$. 20 μL of DPBF ethanol solution (10 mM), 1 μL of H_2O_2 solution (2 M), and 20 μL of MoO_{3-x} NUs (1 mg mL^{-1}) were dispersed in the mixed solution ($V_{ethanol}$:V_{water}=6:4) with a total volume of 2 mL. The generation of $^{\cdot}O_2^-$ was measured at different times (0, 2, 5, 10, 20, and 30 min) by a UV-Vis spectroscopy at 410 nm. Furthermore, excess superoxide dismutase (a $^{\cdot}O_2^-$ scavenger) or carotene (a $^1O_2$ scavenger) was added into this system to investigate the specific kind of ROS. The particle size and the generation of $^{\cdot}O_2^-$ were detected after the storage of MoO_{3-x} NUs in distilled water for 1 d, 3 d, 5 d and 7 d. Moreover, to study the reusability of MoO_{3-x} NUs, the $^{\cdot}O_2^-$ generation was detected by UV-Vis spectroscopy at 410 nm after adding the same amount of H_2O_2 and DPBF into a MoO_{3-x} NUs sample for three times.

In Vitro ·OH Detection. 20 μL of MoO_{3-x} NUs (1 mg mL^{-1}) or 20 μL of MoO_{3-x} NSs (1 mg mL^{-1}), and 1 μL of H_2O_2 (2 M) were added in 3 mL of MB solution (8 μg mL^{-1}). The generation of ·OH was measured at different time points (0, 2, 5, 10, 20, and 30 min) by a UV-Vis spectroscopy at 663 nm.

Cellular Uptake. After surface modification, 0.25 mL of MoO_{3-x} NUs (1 mg mL^{-1}) or MoO_{3-x} NSs (1 mg mL^{-1}) was mixed with 0.25 mL of FITC ethanol solution (10 mg mL^{-1}). After stirring in the dark for 6 h, MoO_{3-x} NUs/FITC or MoO_{3-x} NSs/FITC were washed three times with 50% ethanol solution via centrifugation (10000 rpm, 10 min) to remove free FITC. After washed with PBS (pH 6.0) and DMEM (pH 6.0), MoO_{3-x} NUs/FITC or MoO_{3-x} NSs/FITC were dispersed in DMEM (pH 6.0). B16 melanoma cells were cultured in DMEM supplemented with 10% fetal bovine serum at 37 °C in an atmosphere containing 5% CO_2. B16 cells were seeded on confocal dishes with a glass-bottom insert (Wuxi NEST Biotechnology Co., Ltd, China) and incubated for 12 h. And then the DMEM was replaced with fresh DMEM (pH 6.0) containing MoO_{3-x} NUs/FITC (Mo, 6.25 μg mL^{-1}) or MoO_{3-x} NSs/FITC (Mo, 6.25 μg mL^{-1}). After incubation at 37 °C for 1 h and 4 h, the cells were washed for 3 times with PBS and fixed with 4% paraformaldehyde solution for 30 min. DAPI (dilution 1:20) was then used to visualize the nuclei. Cells were observed by a confocal laser scanning microscope (CLSM; Olympus FV1000, Japan) to confirm the cellular uptake.

Intracellular ROS Detection. The ROS was detected using 2', 7'-dichlorofluorescein-diacetate (DCFH-DA). B16 cells were seeded on confocal dishes with a glass-bottom insert (Wuxi NEST Biotechnology Co., Ltd, China) and incubated for 12 h. And then the DMEM was replaced with fresh DMEM (pH 6.0 or pH 7.4) containing MoO_{3-x} NUs (6.25 μg mL^{-1}) or MoO_{3-x} NSs (6.25 μg mL^{-1}), respectively. After 12 h, the cells were washed and incubated in DCFH-DA working solution (10 μM) at 37 °C for 20 min. The cells were washed with PBS for three times and observed using a CLSM (Olympus FV1000, Japan).

JC-1 Staining. B16 cells were seeded on confocal dishes with a glass-bottom insert (Wuxi NEST Biotechnology Co., Ltd, China) and incubated for 12 h. And then the DMEM was replaced with fresh DMEM (pH 6.0 or pH 7.4) containing MoO_{3-x} NUs (6.25 μg mL^{-1}) or MoO_{3-x} NSs (6.25 μg mL^{-1}), respectively. After 12 h, the cells were washed and incubated in JC-1 working solution at 37 °C for 20 min. The cells were washed with PBS for three times and incubated in Hoechst 33342 solution at 37 °C for 10 min. The cells were washed with PBS for three times, and observed using a CLSM (Olympus IX83-FV3000-OSR, Japan).

Cell Viability Assay. B16 cells or L02 normal liver cells (10^4 cells $well^{-1}$) were seeded in 96 well plates with 200 μL culture medium. After 12 h, cells were treated with DMEM (pH 6.0 or pH 7.4) containing various concentrations of MoO_{3-x} NUs (0, 1.56, 3.125, 6.25, and 12.5 μg mL^{-1}) for 24 h, respectively. The medium was replaced with 200 μL of 10% CCK-8/DMEM solution. After incubation for another 4 h, the absorbance of each well was measured at 450 nm with a microplate reader (ELx800, Bio Tek Instruments Inc., USA). In addition, the cell viability after treatment with NUDPs was also evaluated by the same procedure.

Western Blotting. B16 cells were cultured in DMEM (pH 6.0 or pH 7.4) containing MoO_{3-x} NUs (6.25 μg mL^{-1}) or MoO_{3-x} NSs (6.25 μg mL^{-1}), respectively. After 12 h, B16 cells were collected and lysed in universal lysis buffer (50 mM Tris-HCl, 150 mM NaCl, 2 mM EDTA, 2 mM EGTA, 25 mM NaF, 25 mM β-glycerophosphate pH 7.5, 0.1 mM sodium orthovanadate, 0.1 mM PMSF, 5 μg of leupeptin mL^{-1}, 0.2% Triton X-100, 0.5% Nonidet P-40). Protein concentrations were further determined with the Lowry protein assay. The proteins were separated by SDS-PAGE and transferred to PVDF membranes (IPVH00010, Millipore, Billerica, Massachusetts, USA) and probed with primary antibodies. The primary antibodies were listed as follows: cleaved PARP (1:1000, mouse specific, 9544S), cleaved caspase 3 (1:1000, 9661L) from Cell Signaling Technology (Danvers, Massachusetts, USA); Bcl-2 (1:1000, sc-7382), Bax (1:1000, sc-7480), β-Actin (1:1000, sc-1615) from Santa Cruz Biotechnology (Dallas, USA). Corresponding secondary antibodies (MultiSciences, Hangzhou, China) and ECL (NEL105001EA, PerkinElmer, Ohio, USA) were further incubated to detect enhanced chemiluminescence.

In Vitro and in Vivo Photoacoustic (PA) Imaging. PA signals of MoO_{3-x} NUs and the corresponding NUDPs (2 mg mL^{-1}) at the range from 680 nm to 970 nm were recorded using a Vevo LAZR instrument (Fujifilm, Canada). Then, MoO_{3-x} NUs (10 mg kg^{-1}) were injected into the tumor site and adjacent normal tissue of a BALB/c nude mouse harboring the B16 tumor xenograft. The PA imaging of the BALB/c nude mouse harboring the B16 tumor xenograft was recorded at 5 min, 1 h, 3 h, and 6 h post-injection of MoO_{3-x} NUs at 910 nm using a Vevo LAZR instrument (Fujifilm, Canada). In addition, both tumor and muscle were harvested at 5 min, 1 h, 3 h, and 6 h post-injection of MoO_{3-x} NUs, and digested overnight in 5 mL HNO_3 at 60 °C. After dilution and filtration through a 0.22 μm filter, the Mo levels in sample solutions were quantified by using ICP-MS.

In Vivo Anti-Tumor Treatment. 5×10^6 B16 tumor cells were injected to the back of male BALB/c nude mice. After a week, the BALB/c nude mice harboring a B16 tumor xenograft were randomly divided into three groups (n=5), and were intratumorally injected with PBS, MoO_{3-x} NUs (10 mg kg^{-1}), and MoO_{3-x} NSs (10 mg kg^{-1}) every 3 days, respectively. Tumor volumes (tumor volume=width^2×length/2) and body weights were measured every 2 days. At the end of treatments, tumors and various organs (heart, liver, spleen, lung, and kidney) were harvested for staining (Tumor: hematoxylin & eosin (HE) staining, terminal deoxynucleotidyl transferase dUTP nick end label (TUNEL), and ROS staining; Organs: HE staining). Animal experiments were carried out according to institutional guidelines and were approved by Zhejiang University Laboratory Animal Center.

Hematological and Blood Biochemical Tests. BALB/c mice were intravenously or intramuscularly injected with MoO_{3-x} NUs (5 mg kg^{-1}) to study the tissue toxicity caused by the possible leakage (n=6). Hematological and blood biochemical tests were performed at 0 d, 2 d, and 7 d post-injection.

ASSOCIATED CONTENT

Supporting Information

The Supporting Information is available free of charge on the ACS Publications website at http://pubs.acs.org.

AUTHOR INFORMATION

Corresponding Author

* lingds@zju.edu.cn

Author Contributions

D. L., X. H. and F. L. conceived and designed the study. X. H., F. L., F. X., X. G., N. W. and L. L. performed the experiments. X. H., F. L., F. X., X. G. and L. L. synthesized the materials and detected enzymatic activity. X. H., F. X. and N. W. performed the cell and animal experiments. D.L., X. H., F. L. and F. X. analyzed the data and wrote the manuscript. D.L., F.L., B. Y., K. F. and X. Y. provided project supervision. All the authors discussed the results and approved the final version of the manuscript.

Notes

The authors declare no competing financial interest.

ACKNOWLEDGMENT

We acknowledge financial support by National Key Research and Development Program of China (2016YFA0203600), the National Natural Science Foundation of China (31822019, 51703195, 91859116), "Thousand Talents Program" for Distinguished Young Scholars, the One Belt and One Road International Cooperation Project from Key Research and Development Program of Zhejiang Province (2019C04024), the Zhejiang Provincial Natural Science Foundation of China (LGF19C100002), the Fundamental Research Funds for the Central Universities (2018QNA7020), and Zhejiang Pharmaceutical Association (2019ZYY12).

REFERENCES

(1) Huo, M.; Wang, L.; Chen, Y.; Shi, J. Tumor-selective catalytic nanomedicine by nanocatalyst delivery. *Nat. Commun.* **2017,** *8,* 357.

(2) Wang, Z.; Zhang, Y.; Ju, E.; Liu, Z.; Cao, F.; Chen, Z.; Ren, J.; Qu, X. Biomimetic nanoflowers by self-assembly of nanozymes to induce intracellular oxidative damage against hypoxic tumors. *Nat. Commun.* **2018,** *9,* 3334.

(3) Fan, K.; Xi, J.; Lei, F.; Wang, P.; Zhu, C.; Yan, T.; Xu, X.; Liang, M.; Bing, J.; Yan, X.; Gao, L. In vivo guiding nitrogen-doped carbon nanozyme for tumor catalytic therapy. *Nat. Commun.* **2018,** *9,* 1440.

(4) Lin, L. S.; Song, J.; Song, L.; Ke, K.; Liu, Y.; Zhou, Z.; Shen, Z.; Li, J.; Yang, Z.; Tang, W.; Niu, G.; Yang, H.; Chen, X. Simultaneous fenton-like ion delivery and glutathione depletion by MnO_2-based nanoagent to enhance chemodynamic therapy. *Angew. Chem. Int. Ed.* **2018,** *57,* 4902-4906.

(5) Natalio, F.; André, R.; Hartog, A. F.; Stoll, B.; Jochum, K. P.; Wever, R.; Tremel, W. Vanadium pentoxide nanoparticles mimic vanadium haloperoxidases and thwart biofilm formation. *Nat. Nanotechnol.* **2012,** *7,* 530-535.

(6) Sun, H.; Zhou, Y.; Ren, J.; Qu, X. Carbon nanozymes: enzymatic properties, catalytic mechanism, and applications. *Angew. Chem. Int. Ed.* **2018,** *57,* 9224-9237.

(7) Xia, H.; Li, F.; Hu, X.; Park, W.; Wang, S.; Jang, Y.; Du, Y.; Baik, S.; Cho, S.; Taegyu, K.; Kim, D. H.; Ling, D.; Hui, K. M.; Hyeon, T. pH-sensitive Pt nanocluster assembly overcomes cisplatin resistance and heterogeneous stemness of hepatocellular carcinoma. *ACS Cent. Sci.* **2016,** *2,* 802-811.

(8) Hu, S.; Yi, T.; Huang, Z.; Liu, B.; Wang, J.; Yi, X.; Liu, J. Etching silver nanoparticles using DNA. *Mater. Horiz.* **2019**, *2,* 155-159.
(9) Du, J.; Gu, Z.; Yan, L.; Yong, Y.; Yi, X.; Zhang, X.; Liu, J.; Wu, R.; Ge, C.; Chen, C.; Zhao, Y. Poly(vinylpyrollidone)- and selenocysteine-modified Bi_2Se_3 nanoparticles enhance radiotherapy efficacy in tumors and promote radioprotection in normal tissues. *Adv. Mater.* **2017,** *29,* 1701268.
(10) Wu, J.; Wang, X.; Wang, Q.; Lou, Z.; Li, S.; Zhu, Y.; Qin, L.; Wei, H. Nanomaterials with enzyme-like characteristics (nanozymes): next-generation artificial enzymes (II). *Chem. Soc. Rev.* **2018,** *48,* 1004-1076.
(11) Wei, H.; Wang, E. Nanomaterials with enzyme-like characteristics (nanozymes): next-generation artificial enzymes. *Chem. Soc. Rev.* **2013,** *42,* 6060-6093.
(12) Huang, Y.; Ren, J.; Qu, X. Nanozymes: Classification, Catalytic mechanisms, activity regulation, and applications. *Chem. Rev.* **2019,** *119,* 4357-4412.
(13) Ragg, R.; Tahir, M. N.; Termel, W. Solids Go Bio: Inorganic nanoparticles as enzyme mimics. *Eur. J. Inorg. Chem.* **2016,** *2016,* 1906-1915.
(14) Zhang, Z.; Zhang, X.; Liu, X.; Liu, J. Molecular imprinting on inorganic nanozymes for hundred-fold enzyme specificity. *J. Am. Chem. Soc.* **2017,** *139,* 5412-5419.
(15) Ding, H.; Cai, Y.; Gao, L.; Liang, M.; Miao, B.; Wu, H.; Liu, Y.; Xie, N.; Tang, A.; Fan, K.; Yan, X.; Nie, G. Exosome-like nanozyme vesicles for H_2O_2-responsive catalytic photoacoustic imaging of xenograft nasopharyngeal carcinoma. *Nano Lett.* **2019,** *19,* 203-209.
(16) Wang, X.; Gao, X. J.; Qin, L.; Wang, C.; Song, L.; Zhou, Y.; Zhu, G.; Cao, W.; Lin, S.; Zhou, L.; Wang, K.; Zhang, H.; Jin, Z.; Wang, P.; Gao, X.; Wei, H. e_g occupancy as an effective descriptor for the catalytic activity of perovskite oxide-based peroxidase mimics. *Nat. Commun.* **2019,** *10,* 704.
(17) Zhang, J.; Wu, S.; Lu, X.; Wu, P.; Liu, J. Manganese as a catalytic mediator for photo-oxidation and breaking the pH limitation of nanozymes. *Nano Lett.* **2019,** *19,* 3214-3220.
(18) André, R.; Natálio, F.; Humanes, M.; Leppin, J.; Heinze, K.; Wever, R.; Schröder, H. C.; Müller, W. E. G.; Tremel, W. V_2O_5 nanowires with an intrinsic peroxidase-like activity. *Adv. Funct. Mater.* **2011,** *21,* 501-509.
(19) Cheng, Z.; Zaki, A. A.; Hui, J. Z.; Muzykantov, V. R.; Tsourkas, A. Multifunctional nanoparticles: cost versus benefit of adding targeting and imaging capabilities. *Science* **2012,** *338,* 903-910.
(20) Tibbitt, M. W.; Dahlman, J. E.; Langer, R. Emerging frontiers in drug delivery. *J. Am. Chem. Soc.* **2016,** *138,* 704-717.
(21) Hermann, J. C.; Marti-Arbona, R.; Fedorov, A. A.; Fedorov, E.; Almo, S. C.; Shoichet, B. K.; Raushel, F. M. Structure-based activity prediction for an enzyme of unknown function. *Nature* **2007**, *448,* 775-779.
(22) Romanski, S.; Stamellou, E.; Jaraba, J. T.; Storz, D.; Krämer, B. K.; Hafner, M.; Amslinger, S.; Schmalz, H. G.; Yard, B. A. Enzyme-triggered CO-releasing molecules (ET-CORMs): evaluation of biological activity in relation to their structure. *Free Radical Bio. Med.* **2013,** *65,* 78.
(23) Sheehy, A. M.; Gaddis, N. C.; Malim, M. H. The antiretroviral enzyme APOBEC3G is degraded by the proteasome in response to HIV-1 Vif. *Nat. Med.* **2003,** *9,* 1404-1407.
(24) Ye, E.; Regulacio, M. D.; Zhang, S. Y.; Loh, X. J.; Han, M. Y. Anisotropically branched metal nanostructures. *Chem. Soc. Rev.* **2015,** *44,* 6001-6017.
(25) Narayanan, R.; Tabor, C.; El-Sayed, M. A. Can the observed changes in the size or shape of a colloidal nanocatalyst reveal the nanocatalysis mechanism type: Homogeneous or heterogeneous? *Top. Catal.* **2008,** 48, 60-74.
(26) Ma, L.; Wang, C.; Gong, M.; Liao, L.; Long, R.; Wang, J.; Wu, D.; Zhong, W.; Kim, M. J.; Chen, Y.; Xie, Y.; Xiong, Y. Control over the branched structures of platinum nanocrystals for electrocatalytic applications. *ACS Nano* **2012,** *6,* 9797-9806.
(27) Singh, N.; Savanur, M. A.; Srivastava, S.; D'Silva, P.; Mugesh, G. A redox modulatory Mn_3O_4 nanozyme with multi-enzyme activity provides efficient cytoprotection to human cells in a Parkinson's disease model. *Angew. Chem. Int. Ed.* **2017,** *56,* 14267-14271.
(28) Li, Y.; Cheng, J.; Li, J.; Zhu, X.; He, T.; Chen, R.; Tang, Z. Tunable chiroptical properties from the plasmonic band to metal-ligand charge transfer band of cysteine-capped molybdenum oxide nanoparticles. *Angew. Chem. Int. Ed.* **2018,** *57,* 10236-10240.
(29) Borgschulte, A.; Sambalova, O.; Delmelle, R.; Jenatsch, S.; Hany, R.; Nüesch, F. Hydrogen reduction of molybdenum oxide at room temperature. *Sci. Rep.* **2017,** *7,* 40761.
(30) Tang, W.; Fan, W.; Wang, Z.; Zhang, W.; Zhou, S.; Liu, Y.; Yang, Z.; Shao, E.; Zhang, G.; Jacobson, O.; Shan, L.; Tian, R; Cheng, S.; Lin, L.; Dai, Y.; Shen, Z.; Niu, G.; Xie, J.; Chen, X. Acidity/reducibility dual-responsive hollow mesoporous organosilica nanoplatforms for tumor-specific self-assembly and synergistic therapy. *ACS Nano* **2018,** *12,* 12269-12283.
(31) Song, G.; Hao, J.; Liang, C.; Liu, T.; Gao, M.; Cheng, L.; Hu, J.; Liu, Z. Degradable molybdenum oxide nanosheets with rapid clearance and efficient tumor homing capabilities as a therapeutic nanoplatform. *Angew. Chem. Int. Ed.* **2016,** *55,* 2122-2126.
(32) Zhang, C.; Bu, W.; Ni, D.; Zuo, C.; Cheng, C.; Li, Q.; Zhang, L.; Wang, Z.; Shi, J. A polyoxometalate cluster paradigm with self-adaptive electronic structure for acidity/reducibility-specific photothermal conversion. *J. Am. Chem. Soc.* **2016,** *138,* 8156-8164.
(33) Song, G.; Shen, J.; Jiang, F.; Hu, R.; Li, W.; An, L.; Zou, R.; Chen, Z.; Qin, Z.; Hu, J. Hydrophilic molybdenum oxide nanomaterials with controlled morphology and strong plasmonic absorption for photothermal ablation of cancer cells. *ACS Appl. Mater. Interfaces* **2014,** *6,* 3915-3922.
(34) Jin, M.; He, G.; Zhang, H.; Zeng, J.; Xie, Z.; Xia, Y. Shape-controlled synthesis of copper nanocrystals in an aqueous solution with glucose as a reducing agent and hexadecylamine as a capping agent. *Angew. Chem. Int. Ed.* **2011,** *50,* 10560-10564.
(35) Liu, Q.; Guo, X.; Li, Y.; Shen, W. Synthesis of hollow Co structures with netlike framework. *Langmuir* **2009,** *25,* 6425-6430.
(36) Gong, F.; Cheng, L.; Yang, N.; Jin, Q.; Tian, L.; Wang, M.; Li, Y.; Liu, Z. Bimetallic oxide $MnMoO_x$ nanorods for in vivo photoacoustic imaging of GSH and tumor-specific photothermal therapy. *Nano Lett.* **2018,** *18,* 6037-6044.
(37) Ni, D.; Jiang, D.; Valdovinos, H. F.; Ehlerding, E. B.; Yu, B.; Barnhart, T. E.; Huang, P.; Cai, W. Bioresponsive polyoxometalate cluster for redox-activated photoacoustic imaging-guided photothermal cancer therapy. *Nano Lett.* **2017,** *17,* 3282-3289.
(38) Liu, W.; Li, X.; Li, W.; Zhang, Q.; Bai, H.; Li, J.; Xi, G. Highly stable molybdenum dioxide nanoparticles with strong plasmon resonance are promising in photothermal cancer therapy. *Biomaterials* **2018,** *163,* 43-54.
(39) Long, R.; Mao, K.; Ye, X.; Yan, W.; Huang, Y.; Wang, J.; Fu, Y.; Wang, X.; Wu, X.; Xie, Y.; Xiong, Y. Surface facet of palladium nanocrystals: a key parameter to the activation of molecular oxygen for organic catalysis and cancer treatment. *J. Am. Chem. Soc.* **2013,** *135,* 3200-3207.
(40) Castro, I. A.; Datta, R. S.; Ou, J. Z.; Castellanos-Gomez, A.; Sriram, S.; Daeneke, T.; Kalantar-zadeh, K. Molybdenum oxides-from fundamentals to functionality. *Adv. Mater.* **2017,** *29,* 1701619.
(41) Ni, D.; Jiang, D.; Kutyreff, C. J.; Lai, J.; Yan, Y.; Barnhart, T. E.; Yu, B.; Im, H.-J.; Kang, L.; Cho, S. Y.; Liu, Z.; Huang, P.; Engle, J. W.; Cai, W. Molybdenum-based nanoclusters act as antioxidants and ameliorate acute kidney injury in mice. *Nat. Commun.* **2018,** *9,* 5421.
(42) Kuwahara, Y.; Yoshimura, Y.; Haematsu, K.; Yamashita, H. Mild deoxygenation of sulfoxides over plasmonic molybdenum oxide hybrid with dramatic activity enhancement under visible light. *J. Am. Chem. Soc.* **2018,** *140,* 9203-9210.
(43) Ragg, R.; Natalio, F.; Tahir, M. N.; Janssen, H.; Kashyap, A.; Strand, D.; Strand, S.; Tremel, W. Molybdenum trioxide nanoparticles with intrinsic sulfite oxidase activity. *ACS Nano* **2014,** *8,* 5182-5189.
(44) Narayanan, R.; El-Sayed, M. A. Shape-dependent catalytic activity of platinum nanoparticles in colloidal solution. *Nano Lett.* **2004,** *4,* 1343-1348.
(45) Cuenya, B. R.; Behafarid, F. Nanocatalysis: size- and shape-dependent chemisorption and catalytic reactivity. *Surf. Sci. Rep.* **2015,** *70,* 135-187.

(46) Szatrowski, T. P.; Nathan, C. F. Production of large amounts of hydrogen peroxide by human tumor cells. *Cancer Res.* **1991,** *51,* 794-798.
(47) Pan, L.; Liu, J.; Shi, J. Intranuclear photosensitizer delivery and photosensitization for enhanced photodynamic therapy with ultralow irradiance. *Adv. Funct. Mater.* **2014,** *24,* 7318-7327.
(48) Nathan, C.; Cunningham-Bussel, A. Beyond oxidative stress: an immunologist's guide to reactive oxygen species. *Nat. Rev. Immunol.* **2013,** *13,* 349-361.
(49) Gorrini, C.; Harris, I. S.; Mak, T. W. Modulation of oxidative stress as an anticancer strategy. *Nat. Rev. Drug Discov.* **2013,** *12,* 931-947.
(50) Bao, T.; Yin, W.; Zheng, X.; Zhang, X.; Yu, J.; Dong, X.; Yong, Y.; Gao, F.; Yan, L.; Gu, Z.; Zhao, Y. One-pot synthesis of PEGylated plasmonic $MoO_{(3-x)}$ hollow nanospheres for photoacoustic imaging guided chemo-photothermal combinational therapy of cancer. *Biomaterials* **2016,** 76, 11-24.
(51) Yang, S.; Sun, S.; Zhou, C.; Hao, G.; Liu, J.; Ramezani, S.; Yu, M.; Sun, X.; Zheng, J. Renal clearance and degradation of glutathione-coated copper nanoparticles. *Bioconjugate Chem.* **2015**, *26*, 511-519.

SYNOPSIS TOC